Heliyon 6 (2020) e03259

Contents lists available at ScienceDirect

Heliyon

journal homepage: www.cell.com/heliyon

Research article

Skull diploë is rich in aquaporin-4

Yuji Suzuki [a,*], Hiroki Kitaura [a,b], Yukimi Nakamura [a], Akiyoshi Kakita [b], Vincent J. Huber [a], Nicholas Capozzoli [c], Ingrid L. Kwee [a,d], Tsutomu Nakada [a,d]

[a] Center for Integrated Human Brain Science, Brain Research Institute, University of Niigata, Japan
[b] Department of Pathology, Brain Research Institute, University of Niigata, Japan
[c] Neurology Service, VA Northern California Health Care System, USA
[d] Department of Neurology, University of California, Davis, USA

ARTICLE INFO

Keywords:
Anatomy
Pathology
Medical imaging
Nuclear medicine
Radiology
Tissue culture
Bone
Aquaporin 4 (AQP4)
Skull
Positron emission tomography(PET)
N-(1,3,4-thiadiazol-2-yl) pyridine-3-[11C]-carboxamide ([11C]TGN-020)
Immunohistology

ABSTRACT

Aquaporin-4 (AQP4) is a water conducting membrane integral protein channel which is widely expressed in the astrocyte system of the brain. During the development of the AQP4 positron emission tomography (PET) imaging agent [^{11}C]TGN-020 (*N*-(1,3,4-thiadiazol-2-yl)pyridine-3-[^{11}C]-carboxamide), significant radioligand uptake was observed in the skull, where there was no known distribution of any aquaporin family proteins. Herein we confirmed via a newly developed method for bone-tissue immunohistology, a hitherto unrecognized distribution of AQP4, and not AQP1, in the skull. Other bony structures, by contrast, showed virtually no uptake of [^{11}C]TGN-020, and likewise, do not express either AQP4 or AQP1. Immunohistological analysis demonstrated that the AQP4 expression in the skull is restricted to the diploë. Consequently, we suspect AQP4 plays a pivotal role in the formation and maintenance of yellow marrow and the diploë. However, elucidating the exact nature of that role will require further studies.

1. Introduction

Aquaporin 4 (AQP4) is a pure water conducting channel in the aquaporin family of water and neutral solute transporters (Agre, 2004). While it is widely expressed throughout the human body, AQP4 is most often discussed within the context of its distribution in the central nervous system (CNS) (Jung et al., 1994; Nagelhus and Ottersen, 2013). There, alterations in normal AQP4 distribution have been associated with several disorders, such as post-ischemic cerebral edema, neuromyelitis optica and malignant brain tumors (Huber et al., 2012; Badaut et al., 2014). However, the specific reasons for those reported changes, as well as the roles played by AQP4 in disease progression remain poorly understood. Our laboratory has successfully identified AQP4 ligands that can modulate AQP4 function, allowing for testing potential therapeutic targets, or use as AQP4 imaging agents for investigating changes in AQP4 distribution during disease progression (Huber et al., 2007; Huber et al., 2009a; Huber et al., 2009b). One ligand in particular, *N*-(1,3,4-thiadiazol-2-yl) pyridine-3-[^{11}C]-carboxamide ([^{11}C]TGN-020), was identified as a potentially useful positron emission tomography radioligand for the clinical imaging of AQP4 and AQP1 in the CNS (Nakamura et al., 2011; Suzuki et al., 2013; Suzuki et al., 2018).

Using [^{11}C]TGN-020 for PET imaging, we observed significant radioligand uptake in areas associated with skull (Suzuki et al., 2013). Based on that result, we hypothesized that a previously unidentified pool of aquaporin may be localized in the skull tissues. This communication describes our further findings based on that hypothesis.

2. Methods and materials

2.1. Positron emission tomography

All research involving human subjects was approved in advance by the Internal Review Board of the University of Niigata. Experimental protocols and participant informed consent conformed to the guidelines set forth by the Internal Review Board. This project was registered at the UMIN Clinical Trials Registry as UMIN000005626 (http://www.umin.ac.jp/ctr/index.htm).

* Corresponding author.
E-mail address: yuji-s@bri.niigata-u.ac.jp (Y. Suzuki).

https://doi.org/10.1016/j.heliyon.2020.e03259
Received 3 August 2019; Received in revised form 10 October 2019; Accepted 15 January 2020

2.2. Subjects

Nine healthy male volunteers (one for upper-body, and four each for head and torso imaging), ages 20-24 years, participated in this AQP-PET study. Informed written consent was obtained from all volunteers.

2.3. [^{11}C]TGN-020 synthesis

The radioligand, [^{11}C]TGN-020, was prepared using a TRACERlab FXC Versatile Automated Synthesizer (GE Healthcare, Chicago, IL, USA) as previously detailed (Suzuki et al., 2013). Quality control measurements on all solutions for human injection consisted of pH, chemical purity, radiochemical purity, and endotoxin tests. All [^{11}C]TGN-020 samples used in this study had chemical and radiochemical purities >95%, with radiochemical yields between 400-600 MBq.

2.4. PET imaging

AQP-PET scans were acquired using a combination PET/CT scanner, Discovery ST Elite, (GE Healthcare). Low-dose CT scans were performed in helical mode with 120 kVp, 50 mA, helical thickness of 3.75 mm, and 15 cm field of view (FOV) positioned in the region of the cerebrum or sternum. [^{11}C]TGN-020 (220-250 MBq, 2.9-3.2 MBq/kg body weight) was administered intravenously over a 2 min period by syringe pump (PHD 2000, Harvard Apparatus, Harvard, MA, USA).

PET emission data of the upper body for confirming AQP distribution was acquired starting at 10 min post-administration from the head to the mid-thighs in 6 bed positions, with 10 min per bed position, each with a 51.2 cm axial FOV. Furthermore, PET emission data for analysis of uptake were acquired over 10 min in 3-dimensional statistic mode, starting at 30 min post-administration of the radioligand, with a 25.6 (head) or 51.2 (upper-body and torso) cm axial FOV.

Emission scans were reconstructed with a 128 × 128 × 47 matrix (voxel size equal to 2.0 × 2.0 (head)/4.0 × 4.0 (upper-body and torso) × 3.27 mm) using a 3-dimensional ordered subsets expectation maximization (3D-OSEM) iterative reconstruction algorithm (2 iterations and 28 subsets) after attenuation correction using the CT data.

All PET images were transferred to a Xeleris 3.1 workstation (GE Healthcare) for analysis. Tissue activity concentration was expressed as the standardized uptake value (SUV), g/ml, corrected for body weight and administered dose of radioactivity. Mean SUV ±SD for $n = 4$ individuals was determined at selected regions of interest (ROI) corresponding to skull, rib and upper arm (humerus) bones. Statistical differences between the mean SUVs of individual bone groups were determined by two-tailed T-tests using Prism (Graphpad Software Inc, La Jolla, CA, USA, ver. 6.0).

2.5. Immunohistology

Human tissue samples were obtained via the University of Niigata tissue donor program. Informed consent for participation in this program was obtained from the families of the tissue donor prior to obtaining samples.

Thin slices of skull and rib bone tissue from three patients (77-, 78-, and 81-year-old, women) who died of natural causes were obtained at autopsy. In this study, these slices were decalcified for immunohistochemical staining as follows: Slices were fixed with 20% buffered-formalin for 1 week, and then demineralized by soaking in a 3.75% disodium EDTA solution in distilled water for 2 weeks at 30 °C in a glass container. Subsequently, serial, 4-μm-thick sections were cut and stained. Immunohistochemistry was performed on the sections using primary antibodies against AQP4 (1:500 dilution) (Kitaura et al., 2009), and AQP1 (Abcam, Cambridge, UK; 1:500). Counterstaining was carried out with Mayer's hematoxylin. Negative controls for AQP1 and AQP4 immunohistochemistry was performed using secondary antibodies without either AQP1 or AQP4 antibodies. Kidney tissues treated with the identical technique used for bone decalcification served as positive controls.

3. Results and discussion

AQP-PET images of the upper body clearly demonstrated different [^{11}C]TGN-020 radioligand uptake patterns in skull as compared to the other bones, e.g., vertebrae, rib, humerus, pelvis and femur (Figure 1). The high uptake in the skull, and low uptake in the other bones are in clear contrast with their surrounding tissues, which in the case of muscle, are also a significant pool of AQP4.

Areas with high [^{11}C]TGN-020 uptake corresponding to skull (Figure 2A), and those having considerably lower uptake corresponding to rib and humerus (Figure 2B) were compared. Standard uptake values (SUV) were averaged between 30-40 min post-injection for $n = 4$ volunteers each for head and torso. Mean SUVs were found to be 2.03 ± 0.08, 0.73 ± 0.04 and 0.70 ± 0.04 g/ml, respectively, for areas corresponding to skull, rib and humerus (Figure 2C).

Unfortunately, PET images could not be obtained with sufficient resolution for direct comparison of torso and skull uptake in a single individual due to the inherent limitations of the ligand and instrument. Specifically, the combination of low specific activity and short half-life of ^{11}C, and narrow field of view of the PET instrument precluded such image acquisition. Therefore, four individuals each were selected from the volunteers to receive head or torso PET images, respectively.

Additionally, while [^{11}C]TGN-020 interactions with protein targets outside of the aquaporin family have not been demonstrated, such interactions, or those of its metabolites cannot be ruled out a priori as possible explanations for increased radioligand uptake in skull. Therefore, direct confirmation of AQP4 or AQP1 expression, proteins for which TGN-020 interactions have been demonstrated, was investigated using immunohistology.

Immunohistological staining of decalcified bones itself presents a significant challenge (Alavi et al., 2001). Decalcification in either 10% EDTA for 5 weeks, or Plank-Rychlo's solution for nine days yielded tissue specimens that were unacceptable for immunohistochemical staining.

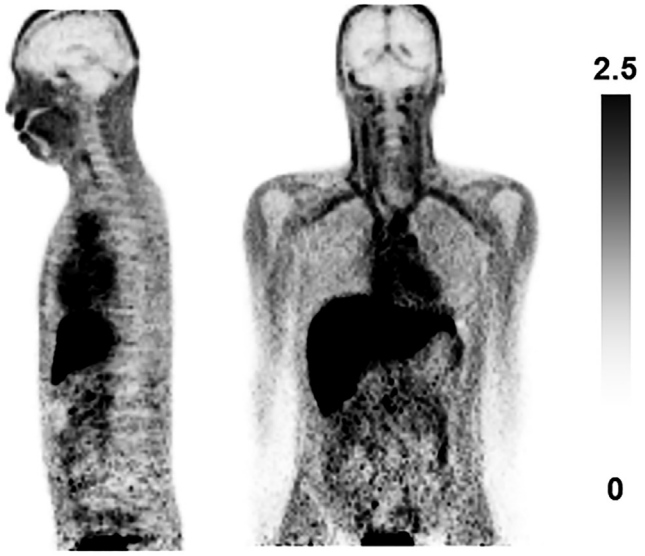

Figure 1. AQP-PET images. AQP-PET images of the upper body, SUV range 0-2.5 g/ml, in sagittal and coronal slices.

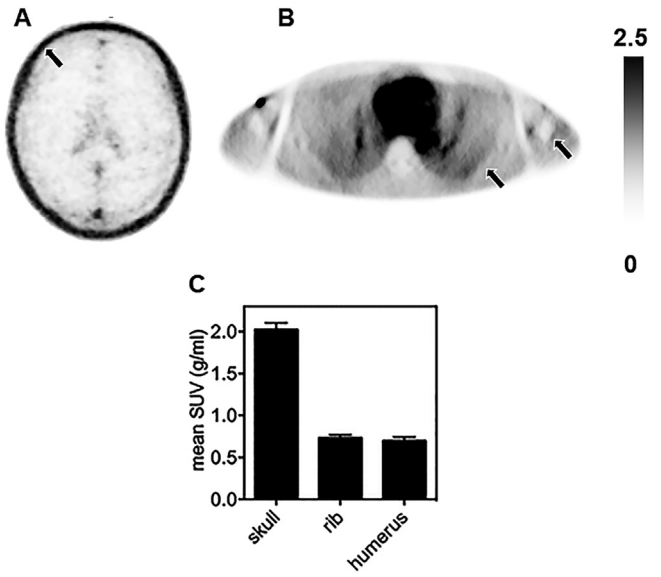

Figure 2. [^{11}C]TGN-020 uptake. Representative AQP-PET images of the head (A), SUV range 0-2.5 g/ml, and representative [^{11}C]TGN-020 PET image of the torso (B), SUV range 0-2.5 g/ml. Approximate location for SUV determination in skull, rib and humerus are indicated with black arrows. (C) Time averaged [^{11}C]TGN-020 uptake SUV of skull, rib and humerus, respectively. Black bars are shown as mean ± SD for $n = 4$ individuals each.

We found, however, that bone specimens treated with 3.5% EDTA for 7 days at 30 °C were suitably decalcified to allow paraffin sectioning, while preserving antigen activity.

Using this modified procedure, skull and rib bone samples obtained at autopsy were tested for the presence of AQP4 and AQP1. We demonstrated negative and positive controls. For the latter, kidney tissue was treated with the identical technique used in bone decalcification (Figure 3a-c). Immunohistochemical staining using the anti-AQP4 antibody revealed that the endosteum lining of the cavity was clearly immunolabeled with the anti-aquaporin-4 antibody (Figure 3g-i). Note, no immunoreactivity was observed with the anti-AQP1 antibody (Figure 3 d-f). Similarly, no immunolabeled structure was observed with either antibody in rib bones (Figure 3j-o).

This study further confirms our prior observation of [^{11}C]TGN-020 uptake difference between skull and long bone, using both [^{11}C]TGN-020 PET (Nakada et al., 2011), and immunohistochemical studies. Aquaporin subtypes are widely distributed in the body, and research indicates AQP9, for example, plays a role in osteoclast development and function (Liu et al., 2009). However, AQP4 was not previously identified as having a significant presence in bone, which makes its apparent abundance in the skull surprising.

The bones of the vertebrate skull derive from both the cranial neural crest and cranial paraxial mesoderm (Holland, 2000). This embryologic difference may explain why skull and brain both express AQP4, while other somatic bones which are derived from more caudal mesoderm, so far as we know, do not. However, it is not simply the skull's proximity to brain that explains its AQP4 expression. Vertebral bodies, which also surround the spinal cord but are derived from caudal body segments, do not demonstrate increased [^{11}C]TGN-020 uptake, and appear unlikely to express AQP4.

The function of this pool of AQP4 remains to be elucidated. Its expression appears limited to the endosteal cells surrounding the diploë, which in turn suggests they are involved in the drying of those spaces. However, while these observations indicate AQP4 plays a role in maintaining the diploë, other potential roles beyond simply removing water from these spaces remain to be determined.

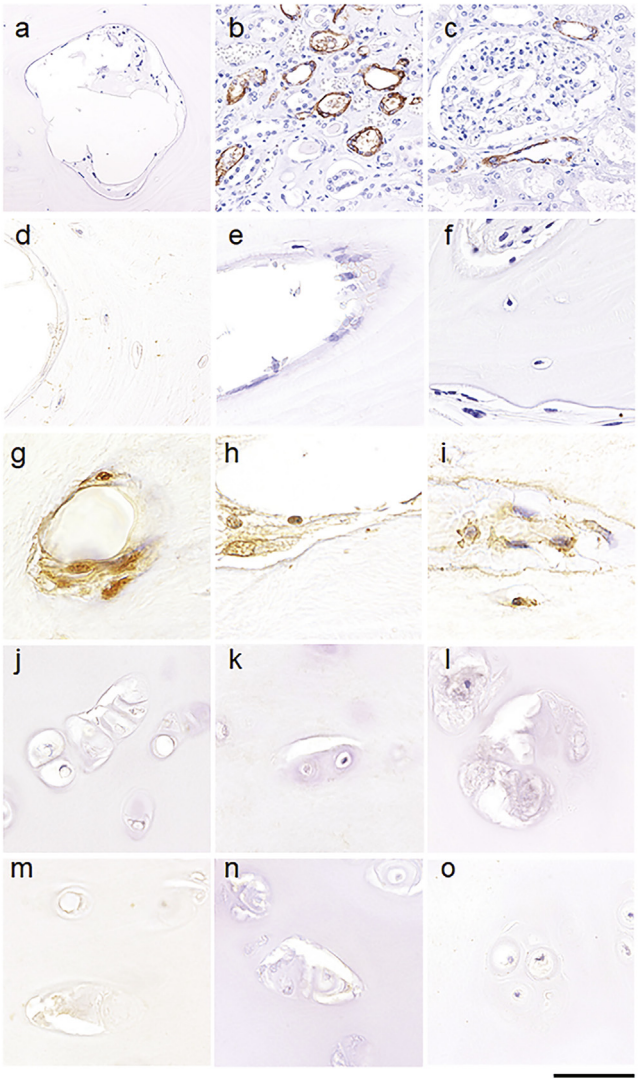

Figure 3. Immunohistology of skull and rib stained with anti-AQP4 and -AQP1 primary antibodies. (a-c) Immunohistology controls for anti-AQP1 and anti-AQP4 immunostaining in kidney tissue; (a) negative control, (b) anti-AQP1 positive control, (c) anti-AQP4 positive control. (d-i) Representative immunostained photomicrographs from individual tissue donors of skull tissue showing diploe medullary cavity and trabeculae; (d-f) anti-AQP1 primary antibody, (g-i) anti-AQP4 primary antibody. (j-o) Representative immunostained photomicrographs from individual tissue donors of rib bone tissue; (j-l) anti-AQP1 primary antibody, (m-o) anti-AQP4 primary antibody. Scale bar, (a-c): 100 μm, (d-o): 50 μm.

Further studies are necessary to uncover those potential roles and their overall significance, and the mechanism by which they occur.

Declarations

Author contribution statement

Y. Suzuki: conceived and designed the experiments; performed the experiments; analyzed and interpreted the data; wrote the paper.

H. Kitarua: performed the experiments; analyzed and interpreted the data.

Y. Nakamura: performed the experiments; contributed reagents, materials, analysis tools or data.

A. Kakita, N. Capozzoli: analyzed and interpreted the data.

V. J. Huber: contributed reagents, materials, analysis tools or data; wrote the paper.

I. L. Kwee: analyzed and interpreted the data; wrote the paper.

T. Nakada: conceived and designed the experiments.

Funding statement

Funding was provided by the Ministry of Education, Culture, Sports, Science and Technology (MEXT), Japan.

Competing interest statement

The authors declare no conflict of interest.

Additional information

No additional information is available for this paper.

References

Agre, P., 2004. Aquaporin water channels (Nobel lecture). Angew. Chem. Int. Ed. 43, 4278–4290.

Alavi, A.M., Dubyak, G.R., Burnstock, G., 2001. Immunohistochemical evidence for ATP receptors in human dental pulp. J. Dent. Res. 80, 476–483.

Badaut, J., Fukuda, A.M., Jullienne, A., Petry, K.G., 2014. Aquaporin and brain diseases. Biochim. Biophys. Acta Gen. Subj. 1840, 1554–1565.

Holland, P.W., 2000. Embryonic development of heads, skeletons and amphioxus: Edwin S. Goodrich revisited. Int. J. Dev. Biol. 44, 29–34.

Huber, V.J., Tsujita, M., Yamazaki, M., Sakimura, K., Nakada, T., 2007. Identification of arylsulfonamides as Aquaporin 4 inhibitors. Bioorg. Med. Chem. Lett 17, 1270–1273.

Huber, V.J., Tsujita, M., Nakada, T., 2009a. Identification of Aquaporin 4 inhibitors using in vitro and in silico methods. Bioorg. Med. Chem. 17, 411–417.

Huber, V.J., Tsujita, M., Kwee, I.L., Nakada, T., 2009b. Inhibition of aquaporin 4 by antiepileptic drugs. Bioorg. Med. Chem. 17, 418–424.

Huber, V.J., Tsujita, M., Nakada, T., 2012. Aquaporins in drug discovery and pharmacotherapy. Mol. Aspect. Med. 33, 691–703.

Jung, J.S., Bhat, R.V., Preston, G.M., Guggino, W.B., Baraban, J.M., Agre, P., 1994. Molecular characterization of an aquaporin cdna from brain - candidate osmoreceptor and regulator of water-balance. Proc. Natl. Acad. Sci. U.S.A. 91, 13052–13056.

Kitaura, H., Tsujita, M., Huber, V.J., Kakita, A., Shibuki, K., Sakimura, K., Kwee, I.L., Nakada, T., 2009. Activity-dependent glial swelling is impaired in aquaporin-4 knockout mice. Neurosci. Res. 64, 208–212.

Liu, Y., Song, L., Wang, Y., Rojek, A., Nielsen, S., Agre, P., Carbrey, J.M., 2009. Osteoclast differentiation and function in aquaglyceroporin AQP9-null mice. Biol. Cell. 101, 133–140.

Nagelhus, E.A., Ottersen, O.P., 2013. Physiological roles of aquaporin-4 in brain. Physiol. Rev. 93, 1543–1562.

Nakada, T., Suzuki, Y., Nakamura, Y., Huber, V., Kwee, I.L., 2011. Skull Is Skull, and Not Simply Another Bony Structure. Abstract. American Neurological Association.

Nakamura, Y., Suzuki, Y., Tsujita, M., Huber, V.J., Yamada, K., Nakada, T., 2011. Development of a novel ligand, [11C]TGN-020, for aquaporin 4 positron emission tomography imaging. ACS Chem. Neurosci. 2, 568–571.

Suzuki, Y., Nakamura, Y., Yamada, K., Huber, V.J., Tsujita, M., Nakada, T., 2013. Aquaporin-4 positron emission tomography imaging of the human brain: first report. J. Neuroimaging 23, 219–223.

Suzuki, Y., Nakamura, Y., Yamada, K., Kurabe, S., Okamoto, K., Aoki, H., Kitaura, H., Kakita, A., Fujii, Y., Huber, V.J., Igarashi, H., Kwee, I.L., Nakada, T., 2018. Aquaporin positron emission tomography differentiates between grade III and IV human astrocytoma. Neurosurgery 82, 842–846.